Numerical analysis of the angular motion of a neutrally buoyant spheroid in shear flow at small Reynolds numbers

T. Rosén,[1,2] J. Einarsson,[3] A. Nordmark,[1] C. K. Aidun,[4] F. Lundell,[1,2] and B. Mehlig[3]
[1]*KTH Mechanics, Royal Institute of Technology, SE-100 44 Stockholm, Sweden*
[2]*Wallenberg Wood Science Center, Royal Institute of Technology, SE-100 44 Stockholm, Sweden*
[3]*Department of Physics, Gothenburg University, SE-41296 Gothenburg, Sweden*
[4]*George W. Woodruff School of Mechanical Engineering and Parker H. Petit Institute for Bioengineering and Bioscience, Georgia Institute of Technology, Atlanta, Georgia 30332-0405, USA*
(Received 20 August 2015; revised manuscript received 3 October 2015; published 22 December 2015)

We numerically analyze the rotation of a neutrally buoyant spheroid in a shear flow at small shear Reynolds number. Using direct numerical stability analysis of the coupled nonlinear particle-flow problem, we compute the linear stability of the log-rolling orbit at small shear Reynolds number Re_a. As $\mathrm{Re}_a \to 0$ and as the box size of the system tends to infinity, we find good agreement between the numerical results and earlier analytical predictions valid to linear order in Re_a for the case of an unbounded shear. The numerical stability analysis indicates that there are substantial finite-size corrections to the analytical results obtained for the unbounded system. We also compare the analytical results to results of lattice Boltzmann simulations to analyze the stability of the tumbling orbit at shear Reynolds numbers of order unity. Theory for an unbounded system at infinitesimal shear Reynolds number predicts a bifurcation of the tumbling orbit at aspect ratio $\lambda_c \approx 0.137$ below which tumbling is stable (as well as log rolling). The simulation results show a bifurcation line in the λ-Re_a plane that reaches $\lambda \approx 0.1275$ at the smallest shear Reynolds number ($\mathrm{Re}_a = 1$) at which we could simulate with the lattice Boltzmann code, in qualitative agreement with the analytical results.

DOI: 10.1103/PhysRevE.92.063022 PACS number(s): 47.15.G−, 83.10.Pp, 47.55.Kf, 47.10.−g

I. INTRODUCTION

The angular motion of a neutrally buoyant spheroid in a simple shear has recently been studied extensively and in detail at moderately large shear Reynolds numbers by numerical stability analysis and by computer simulations using the lattice Boltzmann method [1–7]. Ding and Aidun [1] analyzed rotation in the flow-shear plane and found that a saddle-node bifurcation gives rise to steady states where the symmetry axis of the particle aligns with a certain direction in the flow-shear plane. The authors of Refs. [2–7] analyzed this bifurcation in detail and found a large number of additional bifurcations at intermediate and large Reynolds numbers that give rise to intricate angular dynamics. At zero shear Reynolds number, by contrast, particle and fluid inertia are negligible and the angular dynamics is determined by an infinite set of marginally stable periodic orbits, the so-called Jeffery orbits [8].

The effect of weak fluid and particle inertia on the angular motion of a neutrally buoyant spheroid in an unbounded shear was analyzed recently using perturbation theory [9–13]. In Refs. [10,11] an approximate angular equation of motion was derived for arbitrary aspect ratios of the spheroidal particle, valid to linear order in the shear Reynolds number. Linear stability analysis of the Jeffery orbits subject to infinitesimal inertial perturbations allowed the determination of the linear stability of the log-rolling orbit (where the particle symmetry axis is aligned with vorticity) and of tumbling in the flow-shear plane: Log rolling was found to be unstable for prolate spheroids and stable for oblate spheroids, in agreement with the results obtained by Subramanian and Koch [13] in the slender-body limit. References [10,11] predicted that tumbling in the flow-shear plane is stable for prolate spheroids. For oblate spheroids tumbling was found to be stable for flat disks and otherwise unstable.

This is a problem with a long history [10]. An earlier attempt [14] to compute the stability of log rolling of nearly spherical particles at infinitesimal shear Reynolds number arrived at conclusions at variance with the results stated above, namely, that log rolling is stable for nearly spherical prolate spheroids. Lattice Boltzmann simulations of the problem at moderate shear Reynolds number did not find stable log rolling for prolate spheroids [2,5], but as pointed out in Ref. [5] the shear Reynolds number was not small enough to allow for a definite comparison with theoretical predictions that consider the effect of fluid inertia as an infinitesimal perturbation.

This motivated us to analyze the stability of the log-rolling orbit numerically at small shear Reynolds number Re_a by discretizing the coupled particle-flow problem directly. This method is precise enough at sufficiently small Re_a to determine which theory is correct and for which values of the Reynolds number it applies. We find that the theory of Refs. [10,11] agrees excellently with the simulation results at infinitesimal Re_a when the system size tends to infinity (the theory assumes that the shear is unbounded). Our numerical method allows us to compute the effect of confinement and to estimate the importance of higher-order Re_a corrections to the analytical results for the log-rolling orbit. To analyze the bifurcations of the tumbling orbit at small shear Reynolds numbers we use lattice Boltzmann simulations. At the smallest Re_a attained with the lattice Boltzmann code ($\mathrm{Re}_a = 1$) the bifurcation occurs at a critical aspect ratio of $\lambda_c \approx 0.1275$ in the finite system, in qualitative agreement with the analytical results obtained for an unbounded system.

We briefly comment on the wider context of this paper. Recently there has been a surge of interest in describing the tumbling of small nonspherical particles in turbulent [15–21] and complex flows [22–24] using Jeffery's equation. Studies of the dynamics of larger nonspherical particles in

turbulence [15,20,25] take into account particle inertia but neglect fluid inertia because it is difficult to solve the coupled particle-flow problem. For heavy particles this may be a good approximation, but the results summarized in this paper (and the results of Refs. [4,6,7,10–13]) show that this is approximation is likely to fail for neutrally buoyant and nearly neutrally buoyant particles.

The remainder of this paper is organised as follows. Section II describes the coupled particle-flow problem that is the subject of this paper. In Sec. III we summarize the analytical results of Refs. [10–12] and find the bifurcations of the angular equation of motion obtained in these references. Our numerical results are described in Sec. IV and compared to the analytical results. Section V contains a summary.

II. FORMULATION OF THE PROBLEM

The problem has the following dimensionless parameters. The shape of the spheroid is determined by the shape factor Λ defined as $\Lambda = (\lambda^2 - 1)/(\lambda^2 + 1)$, where λ is the aspect ratio of the spheroid, $\lambda = a/b$ for prolate spheroids, a is the major semiaxis length of the particle, and b is the minor semiaxis length. For oblate spheroids the aspect ratio is defined as $\lambda = b/a$. The effect of fluid inertia is measured by the shear Reynolds number $\mathrm{Re}_a = a^2 s/\nu$, where ν is the kinematic viscosity of the fluid and s is the shear rate. Particle inertia is measured by the Stokes number $\mathrm{St} = (\rho_\mathrm{p}/\rho_\mathrm{f})\mathrm{Re}_a$, where ρ_p and ρ_f are particle and fluid mass densities. The numerical computations described in this paper are performed in a finite system of linear size L and $\kappa = 2a/L$ is a dimensionless measure of the system size, with $2a$ the length of the major axis of the particle.

We use dimensionless variables to formulate the problem. The length scale is taken to be the major semiaxis length a of the spheroid. The velocity scale is as, the pressure scale is μs, the force and torque scales are $\mu s a^2$ and $\mu s a^3$, respectively, and μ is the dynamic viscosity of the fluid. In dimensionless variables the angular equations of motion read

$$\dot{\boldsymbol{n}} = \boldsymbol{\omega} \wedge \boldsymbol{n}, \quad \mathrm{St}\dot{\boldsymbol{L}} = \mathrm{St}(\mathbb{I}\dot{\boldsymbol{\omega}} + \dot{\mathbb{I}}\boldsymbol{\omega}) = \boldsymbol{T}. \tag{1}$$

Here $\boldsymbol{n}$ is the unit vector along the particle symmetry axis, dots denote time derivatives, $\mathbb{I} = A^I(\mathbb{1} - \mathbb{P}_\perp) + B^I\mathbb{P}_\perp$ is the particle-inertia matrix, $\mathbb{P}_\perp$ is a projector onto the plane perpendicular to $\boldsymbol{n}$ with elements $P_{ij} = \delta_{ij} - n_i n_j$, and A^I and B^I are moments of inertia along and orthogonal to $\boldsymbol{n}$. The particle angular velocity is $\boldsymbol{\omega}$ and $\boldsymbol{T}$ is the hydrodynamic torque

$$\boldsymbol{T} = \int_{\mathscr{S}} \boldsymbol{r} \wedge \varpi d\boldsymbol{s}. \tag{2}$$

The integral is over the particle surface $\mathscr{S}$, $\boldsymbol{r}$ is the position vector, and ϖ is the stress tensor with elements $\sigma_{ij} = -p\delta_{ij} + 2S_{ij}$, where p is pressure and S_{ij} are the elements of the strain-rate matrix $\mathbb{S}$, the symmetric part of the matrix $\mathbb{A}$ of fluid-velocity gradients with elements $A_{ij} = \partial_j u_i$ (u_i are the components of the fluid velocity $\boldsymbol{u}$). The antisymmetric part of $\mathbb{A}$ is denoted by $\mathbb{O}$ with elements O_{ij}. To determine the torque it is necessary to solve the Navier-Stokes equations for the incompressible fluid

$$\mathrm{Re}_a[\partial_t \boldsymbol{u} + (\boldsymbol{u}\cdot\boldsymbol{\nabla})\boldsymbol{u}] = -\boldsymbol{\nabla} p + \Delta\boldsymbol{u}, \quad \boldsymbol{\nabla}\cdot\boldsymbol{u} = 0. \tag{3}$$

For a neutrally buoyant particle $\mathrm{Re}_a = \mathrm{St}$.

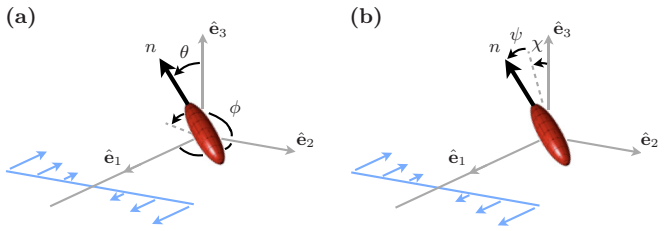

FIG. 1. (Color online) Schematic illustration of a spheroid in a simple shear in a coordinate system that translates with the center of mass of the particle. Vorticity points along the negative $\hat{\mathbf{e}}_3$ axis and $\hat{\mathbf{e}}_1$ is the flow direction. The flow-shear plane is spanned by $\hat{\mathbf{e}}_1$ and $\hat{\mathbf{e}}_2$. We use two different coordinate systems to express the orientation of the unit vector $\boldsymbol{n}$ aligned with the symmetry axis of the particle. (a) Spherical coordinate system used for analyzing linear stability of tumbling in the flow-shear plane. Here θ is the polar angle from the vorticity axis and ϕ is the azimuthal angle in the flow-shear plane. (b) Spherical coordinate system used for analyzing linear stability of log rolling. Here $\boldsymbol{n} = [0,0,1]$ corresponds to $\chi = \psi = 0$.

It is assumed that the slip velocity vanishes on the particle surface $\mathscr{S}$, $\boldsymbol{u} = \boldsymbol{\omega} \wedge \boldsymbol{r}$ when $\boldsymbol{r} \in \mathscr{S}$. The perturbation calculations in Refs. [10–12] apply to a simple shear in an unbounded system and it is assumed that the fluid velocity far from the particle is unaffected by its presence: $\boldsymbol{u} = \boldsymbol{u}^\infty$ as $|\boldsymbol{r}| \to \infty$. Here $\boldsymbol{u}^\infty$ denotes the velocity field of the simple shear $\boldsymbol{u}^\infty = \mathbb{A}^\infty\boldsymbol{r}$ with $A^\infty_{ij} = \delta_{i1}\delta_{j2}$ (see Fig. 1 for an illustration of the geometry). The symmetric and antisymmetric parts of $\mathbb{A}^\infty$ are denoted by $\mathbb{S}^\infty$ and $\mathbb{O}^\infty$, respectively.

The numerical computations described in this paper pertain to a finite system, a cube of linear size $2\kappa^{-1}$ (in dimensionless variables). In the shear direction $u_1 = \pm\kappa^{-1}$ at $r_2 = \pm\kappa^{-1}$. In the flow and vorticity directions periodic boundary conditions are used.

III. THEORY AT SMALL Re_a

In Refs. [10–12] an approximate angular equation of motion for a neutrally buoyant spheroid in an unbounded shear flow was derived, valid to linear order in $\mathrm{Re}_a = \mathrm{St}$:

$$\begin{aligned}\dot{\boldsymbol{n}} = {}& \mathbb{O}^\infty\boldsymbol{n} + \Lambda[\mathbb{S}^\infty\boldsymbol{n} - (\boldsymbol{n}\cdot\mathbb{S}^\infty\boldsymbol{n})\boldsymbol{n}] + \beta_1(\boldsymbol{n}\cdot\mathbb{S}^\infty\boldsymbol{n})\mathbb{P}_\perp\mathbb{S}^\infty\boldsymbol{n} \\ & + \beta_2(\boldsymbol{n}\cdot\mathbb{S}^\infty\boldsymbol{n})\mathbb{O}^\infty\boldsymbol{n} + \beta_3\mathbb{P}_\perp\mathbb{O}^\infty\mathbb{S}^\infty\boldsymbol{n} + \beta_4\mathbb{P}_\perp\mathbb{S}^\infty\mathbb{S}^\infty\boldsymbol{n}.\end{aligned} \tag{4}$$

The first two terms on the right-hand side of this equation are Jeffery's result for a neutrally buoyant spheroid in the creeping-flow limit. The remaining terms are corrections due to particle and fluid inertia. The four coefficients β_α (for $\alpha = 1,\ldots,4$) are linear in Re_a and St but nonlinear functions of the particle aspect ratio λ: $\beta_\alpha = b_\alpha^{(\mathrm{Re}_a)}(\lambda)\mathrm{Re}_a + b_\alpha^{(\mathrm{St})}(\lambda)\mathrm{St}$. These functions were computed by Einarsson *et al.* [10,11] for general values of λ and in Ref. [12] in the nearly spherical limit. Equation (4) determines the effect of small inertial perturbations on the Jeffery orbits. It turns out that log rolling ($\boldsymbol{n}$ aligned with the vorticity axis) and tumbling in the flow-shear plane survive

TABLE I. Asymptotic behavior of the functions $b_\alpha(\lambda) = \beta_\alpha/\mathrm{Re}_a$, where β_α are the coefficients in Eq. (4) for $\mathrm{St} = \mathrm{Re}_a$. The asymptotes are found by expanding the solutions from Refs. [10,11].

b_α	Prolate $\lambda \to \infty$	Oblate $\lambda \to 0$
b_1	$\frac{7}{15(2\ln\lambda-3+\ln 4)} + \frac{-197\ln 2\lambda+92\ln\lambda\ln 4\lambda+106+92(\ln 2)^2}{15\lambda^2(2\ln\lambda-3+\ln 4)^2}$	$\frac{11}{30} + (\frac{176}{45\pi} - \frac{7\pi}{20})\lambda + (-\frac{7}{3} + \frac{3968}{135\pi^2} - \frac{21\pi^2}{80})\lambda^2$
b_2	$\frac{1}{5(2\ln\lambda-3+\ln 4)} + \frac{(\ln\lambda-1+\ln 2)(8\ln 2\lambda-7)}{5\lambda^2(2\ln\lambda-3+\ln 4)^2}$	$\frac{1}{10} + (\frac{8}{15\pi} - \frac{\pi}{20})\lambda + (-\frac{1}{5} + \frac{128}{45\pi^2} - \frac{3\pi^2}{80})\lambda^2$
b_3	$-\frac{4}{5\lambda^2}$	$-\frac{1}{5} + \frac{9\pi^2-64}{60\pi}\lambda + (\frac{3}{5} - \frac{256}{45\pi^2} + \frac{9\pi^2}{80})\lambda^2$
b_4	$\frac{4}{15\lambda^2}$	$-\frac{1}{3} + (\frac{\pi}{20} - \frac{64}{45\pi})\lambda + (\frac{5}{3} - \frac{1024}{135\pi^2} + \frac{3\pi^2}{80})\lambda^2$

small inertial perturbations. In the following two sections we discuss the linear stabilities of these two orbits for $\mathrm{St} = \mathrm{Re}_a$. We write $\beta_\alpha = \mathrm{Re}_a b_\alpha(\lambda)$. Table I gives the asymptotes of these functions for large and small values of the aspect ratio λ. The asymptotes are obtained by expanding the results derived in Ref. [11].

A. Linear stability analysis of log rolling

To analyze the stability of the log-rolling orbit we use the coordinate system shown in Fig. 1(b). The angles χ and ψ are defined so that

$$n_1 = \sin\psi, \quad n_2 = \cos\psi\sin\chi, \quad n_3 = \cos\psi\cos\chi. \tag{5}$$

In these coordinates the equation of motion (4) takes the form

$$\begin{aligned}\dot\psi = {}& \tfrac{1}{8}\{4(\Lambda\cos 2\psi + 1)\sec\psi\sin\chi + [4\beta_1\cos 2\psi\sin^2\chi \\ & + (-2\beta_2 - \beta_3 + \beta_4)\cos 2\chi + 2\beta_2 + 3\beta_3 + \beta_4] \\ & \times \sin\psi\}\cos\psi,\end{aligned} \tag{6a}$$

$$\begin{aligned}\dot\chi = {}& \tfrac{1}{4}\{2(\Lambda - 1)\tan\psi + [(\beta_2 - \beta_1)\cos 2\psi \\ & + \beta_1 - \beta_2 - \beta_3 + \beta_4]\sin\chi\}\cos\chi.\end{aligned} \tag{6b}$$

Log rolling along the vorticity direction $\boldsymbol{n} = [0,0,1]$ corresponds to $\chi = \psi = 0$ and this is a fixed point of Eq. (6) since $\dot\psi = \dot\chi = 0$ in this direction. The stability of this fixed point is determined by the eigenvalues of the linearization of Eq. (6) around this fixed point. To linear order in Re_a the eigenvalues take the form

$$\gamma_{\mathrm{LR}}^{\pm} = \frac{\beta_4}{4} \pm \frac{i}{2}\sqrt{1-\Lambda^2} + o(\mathrm{Re}_a). \tag{7}$$

The real part of this expression was derived in Refs. [10,11] [see, for example, Fig. 3(a) in Ref. [10]]. The coefficient β_4 is linear in Re_a and its sign determines the stability of the log-rolling orbit at infinitesimal Re_a. The coefficient is positive for prolate spheroids (unstable log rolling) and negative for oblate spheroids (stable log rolling). The imaginary part in Eq. (7) shows that the log-rolling fixed point is a spiral at small Re_a. The imaginary part has no correction to linear order in Re_a.

B. Tumbling in the flow-shear plane

Under which circumstances is tumbling in the shear plane stable? In this section we first summarize the results of analytical linear-stability calculations of Refs. [10–12] at infinitesimal Re_a. Second we discuss finite but small shear Reynolds numbers. To analyze tumbling in the flow-shear plane we use the coordinates employed in Refs. [10–12] [illustrated in Fig. 1(a)]

$$n_1 = \sin\theta\cos\phi, \quad n_2 = \sin\theta\sin\phi, \quad n_3 = \cos\theta. \tag{8}$$

In these coordinates the equation of motion (4) takes the form

$$\begin{aligned}\dot\phi = {}& \tfrac{1}{2}(\Lambda\cos 2\phi - 1) + \tfrac{1}{8}\beta_1\sin^2\theta\sin 4\phi \\ & - \tfrac{1}{4}\sin 2\phi(\beta_2\sin^2\theta + \beta_3),\end{aligned} \tag{9a}$$

$$\begin{aligned}\dot\theta = {}& \Lambda\sin\theta\cos\theta\sin\phi\cos\phi \\ & + \tfrac{1}{4}\sin\theta\cos\theta(\beta_1\sin^2\theta\sin^2 2\phi + \beta_3\cos 2\phi + \beta_4).\end{aligned} \tag{9b}$$

This is Eq. (42) in Ref. [10]. Equation (9b) shows that $\dot\theta = 0$ at $\theta = \pi/2$ in the flow-shear plane. The equation of motion for ϕ in this plane is

$$\dot\phi = \tfrac{1}{2}(\Lambda\cos 2\phi - 1) + \tfrac{1}{8}\beta_1\sin 4\phi - \tfrac{1}{4}(\beta_2 + \beta_3)\sin 2\phi. \tag{10}$$

At infinitesimal values of Re_a there is a periodic tumbling orbit in the flow-shear plane because $\dot\phi < 0$. Its linear stability exponent γ_{T} at infinitesimal shear Reynolds numbers was calculated in Refs. [10,11]. It was found that tumbling in the flow-shear plane is stable for prolate particles in this limit and unstable for not too thin oblate particles. For thin platelets tumbling was found to be stable. For infinitesimal shear Reynolds numbers the bifurcation occurs at the critical aspect ratio [10,11]

$$\lambda_{\mathrm{c}} \approx 0.137. \tag{11}$$

This concludes our summary of the results of Refs. [10,11], valid at infinitesimal Re_a.

As Re_a increases we see that $\dot\phi \geqslant 0$ in Eq. (9) for some value(s) of ϕ. This implies the existence of fixed points in the flow-shear plane. This happens in Eq. (9) for any aspect ratio; however, Eq. (9) is valid only to linear order in Re_a. For this reason we only look at limiting cases where Eq. (9) exhibits bifurcations at small values of Re_a. This occurs for thin rods and plates, as will be seen below.

Consider first rods. Rods of infinite aspect ratio align with the flow direction and particles with finite aspect ratio tumble at infinitesimal Re_a. At finite values of Re_a a bifurcation may cause a rod with finite aspect ratio to align. To find this bifurcation point we expand $\dot\phi$ to second order in $1/\lambda$

(Table I) and to second order in ϕ. A double root of the resulting quadratic equation for ϕ determines the bifurcation point:

$$\mathrm{Re}_a^{(c1)} \sim \frac{15}{\lambda}(-3+\ln 4+2\ln\lambda) \quad \text{as } \lambda\to\infty. \tag{12}$$

The leading terms of this result for $\mathrm{Re}_a^{(c1)}$ agree with Eq. (3.31) in Ref. [13] (up to a factor of 8π). Subramanian and Koch [13] derived their result using the slender-body approximation. Note that the qualitative features of the dynamics in the vicinity of $\mathrm{Re}_a^{(c1)}$ are consistent with Eq. (12) in Ref. [1] (see also Ref. [26]). As $\varepsilon \equiv \mathrm{Re}_a - \mathrm{Re}_a^{(c1)}$ tends to zero from below the period of the tumbling orbit tends to infinity as $(-\varepsilon)^{-1/2}$. Above the transition there are two fixed points, a saddle point and a stable node. It follows that the particle aligns at the angle

$$\phi_0 = \frac{1}{\lambda} + \frac{\sqrt{\varepsilon}}{15}\frac{\sqrt{30}}{\sqrt{\lambda(-3+\ln 4+2\ln\lambda)}} + \cdots \quad \text{as } \lambda\to\infty \tag{13}$$

for small values of ε. The form of this equation is consistent with Eqs. (3.30) and (3.31) in Ref. [13].

Now we turn to thin disks. The symmetry vector of an infinitely thin disk aligns with the shear direction, $\dot\phi = 0$ for $\phi = \pi/2$ when $\lambda = 0$. For nonzero values of λ the vector $\boldsymbol{n}$ tumbles in the flow-shear plane in the limit of $\mathrm{Re}_a \to 0$. At finite (but small) values of Re_a a bifurcation may cause the disk to align. To find this bifurcation point we expand $\dot\phi$ to second order in λ (Table I) and to second order in $\delta\phi = \phi - \pi/2$. As above, a double root of the resulting quadratic equation for $\delta\phi$ determines the critical shear Reynolds number

$$\mathrm{Re}_a^{(c2)} \sim 15\lambda \quad \text{as } \lambda\to 0. \tag{14}$$

For $\mathrm{Re}_a > \mathrm{Re}_a^{(c2)}$ the symmetry vector $\boldsymbol{n}$ of the disk aligns in the flow-shear plane at the angle

$$\phi_0 = \frac{\pi}{2} + \lambda + \frac{\sqrt{\epsilon}}{15}\sqrt{30\lambda} \quad \text{as } \lambda\to 0. \tag{15}$$

In deriving this expression only the lowest orders in λ and ϵ were kept.

The bifurcation lines in the λ-Re_a plane given by Eqs. (11), (12), and (14) are shown in Fig. 4. This figure also contains the results of our direct numerical simulations (DNSs), which we discuss next.

IV. NUMERICAL COMPUTATIONS

We performed different types of DNSs of Eqs. (1)–(3) in a finite domain with velocity boundary conditions in the shear direction, periodic boundary conditions in the other directions, and no-slip boundary conditions on the particle surface. We directly computed the linear stability of the log-rolling orbit using version 4.4 of the commercial software package COMSOL MULTIPHYSICS. As explained below, this method could not be used to numerically determine the linear stability of tumbling in the flow-shear plane. Therefore, we used lattice Boltzmann simulations of the particle dynamics to determine the bifurcations of this orbit. To check the accuracy of the lattice Boltzmann simulations we also performed steady-state DNSs using version 9.06 of the commercial software package STAR-CCM+.

A. Direct numerical stability analysis of log rolling at finite values of Re_a

The eigenvalue solver in version 4.4 of the commercial finite-element software package COMSOL MULTIPHYSICS [27] makes it possible to analyze the stability of the log-rolling orbit as described in this section [28]. The symmetries of the problem ensure that log rolling exists not only at infinitesimal but also at finite shear Reynolds numbers.

To determine the linear stability of this orbit it is sufficient to account for small deviations of $\boldsymbol{n}$ from the log-rolling direction $\boldsymbol{n} = [0,0,1]$ and for the fact that the particle spins around its symmetry axis. Thus we avoid computationally expensive remeshing around the particle.

The analysis proceeds in two steps. The first step is to find the steady-state solution of Eqs. (1)–(3) for a given value of Re_a, keeping $\boldsymbol{n}$ fixed at $\boldsymbol{n} = [0,0,1]$. This determines the angular velocity $\boldsymbol{\omega}$ at which the particle spins around its symmetry axis. The second step is to allow for infinitesimal deviations of $\boldsymbol{n}$ and $\boldsymbol{\omega}$ from this steady state. We use a so-called arbitrary Lagrangian-Eulerian method [27] for grid refinement (deformation) close to the particle surface, linearize the resulting dynamics, and determine the eigenvalues of the linearized problem using the eigenvalue solver in COMSOL, which is based on ARPACK FORTRAN routines for large eigenvalue problems [27,29]. The eigenvalue solver provides N eigenvalues $\gamma_1,\ldots,\gamma_N$ closest to the origin in the complex plane, ordered by ascending real parts $\mathrm{Re}(\gamma_1) > \cdots > \mathrm{Re}(\gamma_N)$.

When the shear Reynolds number is small we usually find that $N-2$ eigenvalues $\gamma_3,\ldots,\gamma_N$ are real (within numerical accuracy) with negative real parts. These are fluid modes that decay rapidly as the steady state is approached. In addition, there is one leading pair of complex conjugate eigenvalues $\gamma_{1,2}$ with largest real part. This complex pair corresponds to the linear stability exponent $\gamma_{\mathrm{LR}}^{\pm}$ of the log-rolling orbit. It can have positive or negative real part and the imaginary part determines the angular velocity of the particle. We must choose N large enough to ensure that this pair is among the N eigenvalues the solver finds. In most cases we find $N = 200$ to be sufficient. At larger values of Re_a it may happen that fluid modes have real parts that are larger than that of $\gamma_{\mathrm{LR}}^{\pm}$, yet they are still real (within numerical accuracy). When this happens we verify that the complex pair describes the stability of the orientational dynamics of the particle by numerically integrating the dynamics near the steady state.

In this way we determine $\gamma_{\mathrm{LR}}^{\pm}$ as a function of the particle aspect ratio λ for different degrees κ of confinement and for different values of Re_a. Figure 2 shows real and imaginary parts of $\gamma_{\mathrm{LR}}^{\pm}$ as functions of the aspect ratio of the particle for a small shear Reynolds number ($\mathrm{Re}_a = 2.5\times10^{-4}$) and for different system sizes $\kappa = 0.025$, 0.05, 0.1, and 0.2. Figure 2(a) compares the numerical results for the real part of γ_{LR} with the theory (7). We observe excellent agreement for the largest system ($\kappa = 0.025$). This lends support to the analytical results of Refs. [10–12] and also to the numerical linear stability analysis. As we reduce the system size ($\kappa = 0.05$, 0.1, and 0.2) we observe increasing deviations from the theory for the unbounded system, as expected. For $\kappa = 0.2$ there are substantial finite-size corrections. Figure 2(b) compares numerical results for the imaginary part $\mathrm{Im}(\gamma_{\mathrm{LR}}^{+})$ with Eq. (7). Also for the imaginary part good agreement between the

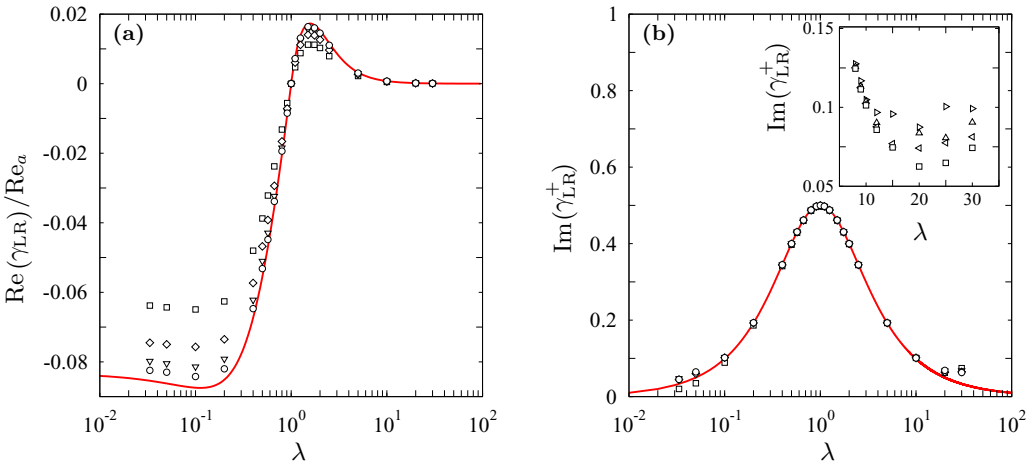

FIG. 2. (Color online) (a) Comparison between the analytical result (7) for $\mathrm{Re}(\gamma_{\mathrm{LR}})$ (solid red line) and numerical results from direct numerical stability analysis (Sec. IV A). The parameters are $\mathrm{Re}_a = 2.5 \times 10^{-4}$, $\kappa = 0.025$ (○), $\kappa = 0.05$ (▽), $\kappa = 0.1$ (◇), and $\kappa = 0.2$ (□). (b) Same comparison for the imaginary part $\mathrm{Im}(\gamma^+_{\mathrm{LR}})$. The inset shows numerical results for $\mathrm{Im}(\gamma^+_{\mathrm{LR}})$ for slender prolate spheroids. Shown are the results for $\kappa = 0.2$, $\mathrm{Re}_a = 2.5 \times 10^{-4}$, and different grid sizes in the vicinity of the particle: the same resolution as in the main plot (□) and characteristic lengths of the finite elements close to the particle larger by a factor of 1.25 (◁), 1.5 (△), and 2 (▷).

numerical results and Eq. (7) is observed for large system sizes, at least for moderate aspect ratios $10^{-1} \leqslant \lambda \leqslant 10$. As for the real part there are finite-size corrections, but they are small relative to the $O(\mathrm{Re}_a^0)$ term in Eq. (7).

Now consider the deviations between the numerical results and theory that can be seen in Fig. 2(b) for more extreme aspect ratios. In this panel [and also in Fig. 2(a)] the size of the finite elements close to the particle surface is chosen as small as possible given the limited computational memory. However, for very large (and also for very small) aspect ratios the resolution is insufficient. This can be seen in the inset of Fig. 2(b). The inset shows data for $\mathrm{Im}(\gamma^+_{\mathrm{LR}})$ for $\kappa = 0.2$ and for different grid resolutions in the vicinity of the particle. For moderate aspect ratios the results converge quickly as the mesh size is reduced; however, for $\lambda > 10$ we do not obtain convergence, reflecting the limitations of the numerical approach.

Figure 3(a) shows finite-Re_a corrections to $\mathrm{Re}(\gamma_{\mathrm{LR}})$ for four different values of λ for the smallest value of κ at which we could reliably compute $\kappa = 0.025$. Theory [30,31] suggests that there are $\mathrm{Re}_a^{3/2}$ corrections to Eq. (7) in the unbounded problem ($\kappa \to 0$). These corrections arise as follows. The leading-order inertial perturbation of the angular dynamics (linear in Re_a) is obtained in terms of the solution of the lowest-order problem, the Stokes problem. At finite but small values of Re_a the Stokes solution provides an accurate description of the fluid velocity in the vicinity of the particle; however, at larger distances from the particle (further away than the Ekman length $2a/\mathrm{Re}_a^{1/2}$) the actual solutions decay more rapidly than the Stokes solution. Within the perturbative scheme used in Refs. [10–13] this gives rise to a $\mathrm{Re}_a^{3/2}$ correction. The precise form of higher-order Re_a-corrections is not known. We assume that the next order is quadratic in Re_a and compare the Re_a dependence observed in the direct numerical simulations with a fit of the form

$$\mathrm{Re}(\gamma_{\mathrm{LR}}) = a_1(\lambda,\kappa)\mathrm{Re}_a + a_2(\lambda,\kappa)\mathrm{Re}_a^{3/2} + a_3(\lambda,\kappa)\mathrm{Re}_a^2 + \cdots . \tag{16}$$

The values obtained for the coefficients a_1, a_2, and a_3 are listed in Table II. The data shown in Fig. 3(a) and Table II are consistent with the existence of $\mathrm{Re}_a^{3/2}$ corrections when the system is large enough $\kappa \ll \mathrm{Re}_a^{1/2}$.

Figure 3(b) shows finite-size corrections to $\mathrm{Re}(\gamma_{\mathrm{LR}})$ for $\mathrm{Re}_a = 2.5 \times 10^{-4}$ and for four different values of λ. Also shown are fits of the form

$$\mathrm{Re}(\gamma_{\mathrm{LR}})/\mathrm{Re}_a = c_1(\lambda) + c_2(\lambda)\kappa + c_3(\lambda)\kappa^2. \tag{17}$$

The resulting coefficients are given in Table III. We see from Fig. 3(b) that the fits describe the numerically observed finite-size dependence accurately, but Eq. (17) is just an ansatz. Also shown are linear approximations valid at small κ. We see that the finite-size effects are to a good approximation linear in κ for the data shown for $\kappa \leqslant 0.1$. Table III shows that the limiting values c_1 obtained as $\kappa \to 0$ are in excellent agreement with the theoretical results for the unbounded system.

B. Time-resolved lattice Boltzmann simulations

To analyze the bifurcations of the tumbling in the flow-shear plane we use the lattice Boltzmann method with external boundary force [32]. To restrict the computational time, the domain size is set to a maximum of 240 lattice units. This allows us to resolve the particle with at least six fluid grid nodes along its smallest dimension, with system size $\kappa = 0.2$. These choices limit the range of aspect ratios that can be

TABLE II. Coefficients a_1, a_2, and a_3 from the fit of Eq. (16) to the data in Fig. 3(a) for $\kappa = 0.025$.

λ	a_1	a_2	a_3
1/4	−0.0830	0.0652	−0.0200
1/2	−0.0566	0.0482	−0.0183
2	0.0155	−0.0125	0.0035
4	0.0051	−0.0039	0.0008

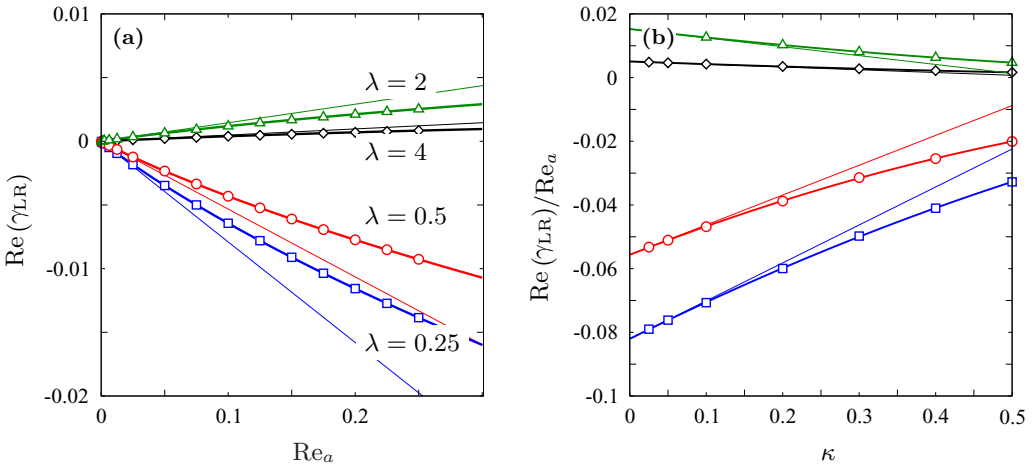

FIG. 3. (Color online) (a) Plot of $\mathrm{Re}(\gamma_{\mathrm{LR}})$ as a function of Re_a for $\kappa = 0.025$ and for four different values of λ. The thin solid lines show the limiting behavior as $\mathrm{Re}_a \to 0$. The thick solid lines show fits to Eq. (16). The coefficients are given in Table II. (b) Finite-size corrections to $\mathrm{Re}(\gamma_{\mathrm{LR}})/\mathrm{Re}_a$ for $\mathrm{Re}_a = 2.5 \times 10^{-4}$ and for the same values of λ as in (a). The thick solid lines show quadratic fits to the small-κ behavior and thin solid lines show the corresponding linear κ dependence for small values of κ.

simulated to $\lambda \in [1/8,8]$. We take Re_a larger than or equal to unity in our simulations. This is because it is computationally very expensive to reach small values of the shear Reynolds number, as discussed by Rosén *et al.* [6,7].

To estimate the critical aspect ratio λ_c where tumbling changes stability for oblate particles we proceed as follows. We initialize the particle at rest, close to the tumbling orbit at $\phi = \pi/2$ and $\theta = \pi/2 - \delta\theta$ with $\delta\theta = 0.017$. We integrate the dynamics for aspect ratios $\lambda = 1/8,1/7,1/6,1/5,1/4$ and for Re_a between 1 and 10 with unit increments. We determine whether the trajectory tends to tumbling in the flow-shear plane or to the log-rolling orbit and determine the location of the bifurcation by interpolation. At $\mathrm{Re}_a = 1$ we run simulations for λ ranging between 0.125 and 0.160 with increments of 0.05 and determine the bifurcation point by linear interpolation. The results are illustrated in Fig. 4. We see that the results agree fairly well with Eq. (11). At the smallest value of Re_a simulated with the lattice Boltzmann code, the transition occurs at $\lambda_c \approx 0.1275$, not too far from the analytical result (11) at infinitesimal Re_a for the unbounded system.

Using lattice Boltzmann simulations, we also obtain estimates for $\mathrm{Re}_a^{(c1)}$ and $\mathrm{Re}_a^{(c2)}$ (Sec. III). This is done by initializing the particle at rest at $\phi = \pi/4$ and $\theta = \pi/2$ for $\lambda > 1$ and at $\phi = 3\pi/4$ and $\theta = \pi/2$ for $\lambda < 1$. We then determine whether the particle tends to a steady state or continues to tumble and determine the critical Reynolds number by linear interpolation. The results of these simulations are also shown in Fig. 4 and are compared with the analytical results for thin disks and rods given by Eqs. (12) and (14). We find that the agreement

TABLE III. Coefficients c_1, c_2, and c_3 from the fit of Eq. (17) to the data in Fig. 3(b). Also given are the numerical values of $b_4(\lambda)/4$ to which the coefficient c_1 should converge as $\kappa \to 0$ and $\mathrm{Re}_a \to 0$. These values are taken from Ref. [10] since the aspect ratios $\lambda = 1/4,1/2,2,4$ are not small (large) enough to use the asymptotic formulas given in Table I.

λ	c_1	$b_4(\lambda)/4$	c_2	c_3
1/4	−0.08205	−0.0820	0.11923	−0.04124
1/2	−0.05564	−0.0555	0.09373	−0.04521
2	0.01526	0.0153	−0.02784	0.01347
4	0.00510	0.0051	−0.00870	0.00367

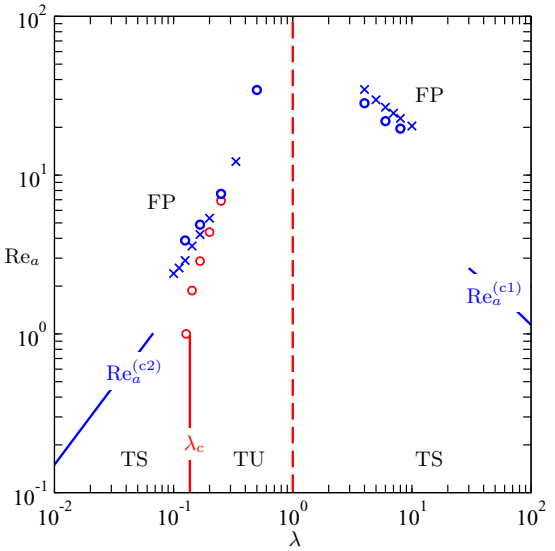

FIG. 4. (Color online) Bifurcations of the tumbling orbit in the flow-shear plane. Bifurcation lines derived in Sec. III for the unbounded system [Eqs. (12), (14), and (11)] are shown as solid lines. The label TS indicates that tumbling is stable, TU that it is unstable, and FP that the tumbling orbit has bifurcated giving rise to a fixed orientation in the flow-shear plane. The dashed line denotes the symmetry line at $\lambda = 0$ where the tumbling orbit changes stability. Numerical results for the finite system ($\kappa = 0.2$) are shown as symbols: circles denote results from the time-resolved lattice Boltzmann simulations described in Sec. IV B and crosses represent results from the steady-state simulations described in Sec. IV C. The bifurcations where tumbling in the flow-shear plane changes stability are shown in red and the bifurcations where stable tumbling in the flow-shear plane changes to a stable fixed point are shown in blue.

is only qualitative. This is not surprising since Eqs. (12) and (14) are based on Eq. (4), which is valid only to linear order in Re_a and cannot be expected to describe the dynamics at Reynolds numbers of order unity or larger. We also note that the lattice Boltzmann simulations were performed for a rather small system, while the analytical results pertain to an unbounded system. Figures 2(a) and 3(b) show that there are substantial finite-size corrections to the stability exponent of the log-rolling orbit in the finite system for $\kappa = 0.2$. We therefore expect that there are equally important finite-size corrections to the locations of the bifurcations in Fig. 4; however, at present we cannot perform lattice Boltzmann simulations for larger systems with sufficient resolution to quantify this statement. In order to check the accuracy of the lattice Boltzmann simulations at $\kappa = 0.2$ we determined the critical Reynolds numbers $\mathrm{Re}_a^{(c1)}$ and $\mathrm{Re}_a^{(c2)}$ using an alternative approach, described in the next section.

C. Steady-state simulations using STAR-CCM+

We compute the critical Reynolds numbers $\mathrm{Re}_a^{(c1)}$ and $\mathrm{Re}_a^{(c2)}$ using version 9.06 of the commercial finite-volume software package STAR-CCM+ [33]. We choose the same system size as in the lattice Boltzmann simulations $\kappa = 0.2$. The particle orientation is fixed at $\theta = \pi/2$ and $\phi \in [0,\pi/2]$ for prolate particles and $\phi \in [\pi/2,\pi]$ for oblate particles. For a given particle aspect ratio λ and value of Re_a we compute the steady-state torque on the particle. If the torque vanishes, the chosen particle orientation is a fixed point for the given parameters. A fixed particle orientation makes it possible to use a very fine local grid around the particle. For different choices of ϕ we find critical Reynolds numbers where the steady-state torque vanishes. The minimum of this critical Reynolds as a function of ϕ gives $\mathrm{Re}_a^{(c1)}$ and $\mathrm{Re}_a^{(c2)}$ for prolate and oblate particles, respectively. The corresponding results for $\mathrm{Re}_a^{(c1)}$ and $\mathrm{Re}_a^{(c2)}$ are also shown in Fig. 4. We conclude that the lattice Boltzmann simulations slightly underestimate the critical value $\mathrm{Re}_a^{(c1)}$, while they slightly overestimate $\mathrm{Re}_a^{(c2)}$.

V. CONCLUSION

Using numerical linear stability analysis we computed the stability of the log-rolling orbit of a neutrally buoyant spheroid in a simple shear at small Re_a. For infinitesimally small Re_a in the unbounded system this problem was recently solved for arbitrary aspect ratios using perturbation theory in the shear Reynolds number. The fact that both calculations agree in the limits $\mathrm{Re}_a \to 0$ and $\kappa \to 0$ (unbounded system) lends support to the analytical calculations [10–12], but also to the numerical linear stability analysis described in the present article. In the limit of large system size ($\kappa \to 0$) we found that there are corrections to the analytical result for the exponent $\mathrm{Re}(\gamma_{\mathrm{LR}})$ that are consistent with terms of order $\mathrm{Re}_a^{3/2}$. We also investigated finite-size corrections to $\mathrm{Re}(\gamma_{\mathrm{LR}})$ at small Re_a and found that they are substantial. It would be of interest to calculate both finite-Re_a and finite-size corrections to $\mathrm{Re}(\gamma_{\mathrm{LR}})$ by extending the method used in Refs. [10–12].

We did not investigate the stability of the tumbling orbit with numerical linear stability analysis because the required remeshing is computationally very expensive. Instead we studied the stability of tumbling in the flow-shear plane using lattice Boltzmann simulations. We tracked the bifurcation line between stable and unstable tumbling for thin oblate spheroids (solid red line in Fig. 4) down to as small values of Re_a as we could reliably achieve and found that the transition occurs at $\lambda_c \approx 0.1275$ at $\mathrm{Re}_a = 1$, in fair agreement with the theoretical prediction 0.137.

Finally, we determined for which values of λ and Re_a tumbling in the flow-shear plane bifurcates to a fixed point, using lattice Boltzmann simulations, and also by numerically computing steady-state torques using STAR-CCM+. The two numerical procedures give results that are in fairly good agreement with each other, yet the agreement with the analytical results (12) and (14) is only qualitative.

Detailed analysis of the lattice Boltzmann dynamics near the bifurcation at $\mathrm{Re}_a^{(c2)}$ reveals the phase-space topology near the bifurcation at moderate Reynolds numbers ($\mathrm{Re}_a^{(c2)} \approx 7.8$ at $\lambda = 1/4$) [see Figs. 3(d) and 3(e) in Ref. [7]]. For $\lambda = 1/4$ a second transition occurs at $\mathrm{Re}_a^{(c3)} \approx 5$ where the log-rolling orbit changes from stable spiral to stable node. Equation (4) also exhibits this transition. However, since Eq. (4) is valid to linear order in Re_a, the bifurcation can only be analyzed in the limit $\lambda \to 0$. We find that the two transitions occur in reverse order: The tumbling to fixed point bifurcation occurs before the spiral to node transition as the shear Reynolds number is increased. There are several possible explanations for these subtle differences. They could be due to higher-order Re_a corrections to Eq. (4) such as the $\mathrm{Re}_a^{3/2}$ corrections alluded to above. However, we have also observed (not shown) in the numerical simulations of the bounded system that $\mathrm{Re}_a^{(c3)}$ increases as κ becomes smaller. In the limit of $\kappa \to 0$ we expect that the order of the transitions agrees with the prediction for the unbounded system. In summary, we can conclude that the results of our numerical computations agree well with the theoretical predictions at infinitesimal Reynolds numbers: We find excellent agreement for the stability exponent of the log-rolling orbit and the bifurcation of the tumbling orbit for thin oblate particles occurs in both theory and simulations at similar values of λ_c. However, there are a number of subtle differences between theory and simulations at larger Reynolds numbers. At present we cannot reliably perform lattice Boltzmann simulations at much smaller Reynolds numbers than those shown in Fig. 4 and it is very difficult to perform such simulations at still smaller values of κ. Therefore, it would be of great interest to extend the analytical calculations to include $\mathrm{Re}_a^{3/2}$ corrections and to account for finite-size effects.

ACKNOWLEDGMENTS

J.E. and B.M. acknowledge support by Vetenskapsrådet and by the grant "Bottlenecks for particle growth in turbulent aerosols" from the Knut and Alice Wallenberg Foundation, Grant No. KAW 2014.0048. T.R. and F.L. acknowledge financial support from the Wallenberg Wood Science Center, Bengt Ingeström's Foundation, and Ångpanneföreningen's Foundation for Research and Development. Support from the MPNS COST Action No. MP1305 "Flowing matter" is gratefully acknowledged. The simulations were performed using resources provided by the Swedish National Infrastructure for

Computing at the High Performance Computing Center North and at the National Supercomputer Center in Sweden. We also acknowledge the help from E. Sundström in setting up the simulations using STAR-CCM+.

[1] E.-J. Ding and C. K. Aidun, The dynamics and scaling law for particles suspended in shear flow with inertia, J. Fluid Mech. **423**, 317 (2000).
[2] D. Qi and L. Luo, Rotational and orientational behavior of three-dimensional spheroidal particles in Couette flows, J. Fluid Mech. **477**, 201 (2003).
[3] H. Huang, X. Yang, M. Krafczyk, and X.-Y. Lu, Rotation of spheroidal particles in Couette flows, J. Fluid Mech. **692**, 369 (2012).
[4] T. Rosén, F. Lundell, and C. K. Aidun, Effect of fluid inertia on the dynamics and scaling of neutrally buoyant particles in shear flow, J. Fluid Mech. **738**, 563 (2014).
[5] W. Mao and W. Alexeev, Motion of spheroid particles in shear flow with inertia, J. Fluid Mech. **749**, 145 (2014).
[6] T. Rosén, M. Do-Quang, C. K. Aidun, and F. Lundell, The dynamical states of a prolate spheroidal particle suspended in shear flow as a consequence of particle and fluid inertia, J. Fluid Mech. **771**, 115 (2015).
[7] T. Rosén, M. Do-Quang, C. K. Aidun, and F. Lundell, Effect of fluid and particle inertia on the rotation of an oblate spheroidal particle suspended in linear shear flow, Phys. Rev. E **91**, 053017 (2015).
[8] G. B. Jeffery, The motion of ellipsoidal particles immersed in a viscous fluid, Proc. R. Soc. London Ser. A **102**, 161 (1922).
[9] J. Einarsson, J. R. Angilella, and B. Mehlig, Orientational dynamics of weakly inertial axisymmetric particles in steady viscous flows, Physica D **278–279**, 79 (2014).
[10] J. Einarsson, F. Candelier, F. Lundell, J. R. Angilella, and B. Mehlig, Rotation of a spheroid in a simple shear at small Reynolds number, Phys. Fluids **27**, 063301 (2015).
[11] J. Einarsson, F. Candelier, F. Lundell, J. R. Angilella, and B. Mehlig, Effect of weak fluid inertia upon Jeffery orbits, Phys. Rev. E **91**, 041002(R) (2015).
[12] F. Candelier, J. Einarsson, F. Lundell, B. Mehlig, and J. R. Angilella, The role of inertia for the rotation of a nearly spherical particle in a general linear flow, Phys. Rev. E **91**, 053023 (2015).
[13] G. Subramanian and D. L. Koch, Inertial effects on fibre motion in simple shear flow, J. Fluid Mech. **535**, 383 (2005).
[14] P. G. Saffman, On the motion of small spheroidal particles in a viscous liquid, J. Fluid Mech. **1**, 540 (1956).
[15] C. Marchioli, M. Fantoni, and A. Soldati, Orientation, distribution, and deposition of elongated, inertial fibers in turbulent channel flow, Phys. Fluids **22**, 033301 (2010).
[16] S. Parsa, E. Calzavarini, F. Toschi, and G. A. Voth, Rotation Rate of Rods in Turbulent Fluid Flow, Phys. Rev. Lett. **109**, 134501 (2012).
[17] A. Pumir and M. Wilkinson, Orientation statistics of small particles in turbulence, New J. Phys. **13**, 093030 (2011).
[18] R. Ni, N. T. Ouelette, and G. A. Voth, Alignment of vorticity and rods with Lagrangian fluid stretching in turbulence, J. Fluid Mech. **743**, R3 (2014).
[19] L. Chevillard and C. Meneveau, Orientation dynamics of small, triaxial-ellipsoidal particles in isotropic turbulence, J. Fluid Mech. **737**, 571 (2013).
[20] N. R. Challabotla, L. Zhao, and H. Andersson, Orientation and rotation of inertial disk particles in wall turbulence, J. Fluid Mech. **766**, R2 (2015).
[21] M. Byron, J. Einarsson, K. Gustavsson, G. Voth, B. Mehlig, and E. Variano, Shape-dependence of particle rotation in isotropic turbulence, Phys. Fluids **27**, 035101 (2015).
[22] M. Wilkinson, V. Bezuglyy, and B. Mehlig, Fingerprints of random flows, Phys. Fluids **21**, 043304 (2009).
[23] V. Bezuglyy, B. Mehlig, and M. Wilkinson, Poincaré indices of rheoscopic visualisations, Europhys. Lett. **89**, 34003 (2010).
[24] M. Wilkinson, V. Bezuglyy, and B. Mehlig, Emergent order in rheoscopic swirls, J. Fluid Mech. **667**, 158 (2011).
[25] K. Gustavsson, J. Einarsson, and B. Mehlig, Tumbling of Small Axisymmetric Particles in Random and Turbulent Flows, Phys. Rev. Lett. **112**, 014501 (2014).
[26] C. M. Zettner and M. Yoda, Moderate-aspect-ratio elliptical cylinders in simple shear with inertia, J. Fluid Mech. **442**, 241 (2001).
[27] COMSOL MULTIPHYSICS Reference Manual, version 4.4, 2013, www.comsol.com
[28] T. Rosén, A. Nordmark, C. K. Aidun, and F. Lundell (unpublished).
[29] http://www.caam.rice.edu/software/ARPACK
[30] P. Lovalenti and J. Brady, The force on a bubble, drop or particle in arbitrary time-dependent motion at small Reynolds number.Phys. Fluids **5**, 2104 (1993).
[31] F. Candelier, J.-R. Angilella, and M. Souhar, On the effect of inertia and history forces on the slow motion of a spherical solid or gaseous inclusion in a solid-body rotation flow, J. Fluid Mech. **545**, 113 (2005).
[32] J. Wu and C. K. Aidun, Simulating 3D deformable particle suspensions using lattice Boltzmann method with discrete external boundary force, Int. J. Numer. Methods H. **62**, 765 (2010).
[33] *STAR- CCM+ Reference Manual, version 9.06*, 2014, www.cd-adapco.com